



HAL
open science

Analysis of water transport in unsaturated conditions comparison between labcrete and fieldcrete

Stéphane Poyet, B. Bary, E. Coppens

► **To cite this version:**

Stéphane Poyet, B. Bary, E. Coppens. Analysis of water transport in unsaturated conditions comparison between labcrete and fieldcrete. *Construction and Building Materials*, 2019, 205, 10.1016/j.conbuildmat.2019.02.034 . cea-02339768

HAL Id: cea-02339768

<https://cea.hal.science/cea-02339768>

Submitted on 21 Oct 2021

HAL is a multi-disciplinary open access archive for the deposit and dissemination of scientific research documents, whether they are published or not. The documents may come from teaching and research institutions in France or abroad, or from public or private research centers.

L'archive ouverte pluridisciplinaire **HAL**, est destinée au dépôt et à la diffusion de documents scientifiques de niveau recherche, publiés ou non, émanant des établissements d'enseignement et de recherche français ou étrangers, des laboratoires publics ou privés.



Distributed under a Creative Commons Attribution - NonCommercial 4.0 International License

1 **Analysis of water transport in unsaturated conditions:** 2 **comparison between labcrete and fieldcrete**

3 Stéphane POYET¹, Benoit BARY¹, Erik Coppens²

4 ¹ Den-Service d'Etude du Comportement des Radionucléides (SECR), CEA, Université Paris-
5 Saclay, F-91191, Gif-sur-Yvette, France

6 ² ONDRAF-NIRAS, 14 Avenue des Arts, B-1210 Brussels, Belgium

7 **Corresponding author:** Stéphane POYET, stephane.poyet@cea.fr

8 **Abstract**

9 The differences in unsaturated permeability between concrete prepared in the laboratory
10 (labcrete) and on a real construction site (fieldcrete) were investigated experimentally and
11 using inverse analysis. Although more porous, the fieldcrete specimens were shown to have an
12 average permeability very close to the labcrete ones. The fieldcrete permeabilities also exhibited
13 more variability than the labcrete ones. Numerical simulations performed on 3D reconstructed
14 concrete specimens showed that differences in coarse aggregate distribution cannot explain the
15 variability observed at the macroscopic scale and that an important part may originate from the
16 properties of mortar matrix.

17 **Keywords:** labcrete; fieldcrete; permeability; inverse analysis; 3D mesostructure.

18 **1. Introduction**

19 The amount of evaporable water that is present in the porosity of concrete is of paramount
20 importance for the durability of reinforced concrete structures: (1) because it influences the
21 concrete transport properties and then the ingress rate of aggressive species such as CO₂ or
22 chlorides [1–5]; (2) because the poral solution is the medium that allows chemical reactions to

23 occur such as carbonation or rebar corrosion [6–8] and also (3) because the loss of water
24 induces shrinkage and possibly cracking [9–11] Describing water exchange between a concrete
25 structure and the surrounding environment is then the first and inevitable step towards
26 durability assessment.

27 Among the data needed to describe water transport, the permeability is of first importance: it
28 accounts for the ability of a fluid (water in our case) to pass through concrete due to pressure
29 gradient. Permeability is considered as a relevant durability index for service-life prediction
30 [12–16] and is measured to verify whether the concrete composition complies with the
31 specifications. To this end, characterization tests are generally performed using specimens
32 prepared in the laboratory ('labcrete'). This approach may be regarded as inconsistent because
33 it does not account for the properties of the concrete that is prepared and used onsite
34 ('fieldcrete') [17,18]. Labcrete specimens are generally prepared with great care by experienced
35 technicians and/or scientists using batches of small volume, in controlled environmental
36 conditions and are carefully vibrated and cured whereas fieldcrete is generally prepared in
37 much larger batches in concrete plants in uncontrolled environmental conditions before further
38 use by onsite workers [18,19]. Fieldcretes are then likely to be of lower quality than labcretes in
39 terms of mechanical as well as durability properties; the question is how much?

40 There are very few studies in the literature that compare the properties of labcrete and
41 fieldcrete. However, fieldcretes are known to exhibit reduced compressive strength compared to
42 labcretes and the difference is about 10-15% [20,21]. Unexpectedly, no significant differences in
43 chloride diffusion coefficient between laboratory and field measurements were obtained over a
44 large panel of concretes by [22,23], indicating that fieldcretes and labcretes would be similar in
45 terms of diffusion properties. The available results about permeability tell a different story.
46 Using gas, the permeability of fieldcrete was shown to be greater than that of the labcrete up to
47 four times [24–26]. The same applies to the studies of Diaz *et al.* [27] who used the Torrent
48 permeameter to measure the permeability of low-carbon concrete elements exposed to marine
49 environment *in situ* as well as companion specimens in the laboratory. The field measurements

50 were up to 8 times higher than the laboratory ones. This discrepancy may be due to differences
51 in properties of lab- and fieldcrete but also to differences in water content between the
52 laboratory and field specimens [28] and to the absence of proper cure for the fieldcrete [29,30].
53 The objective of this study is to investigate the differences in water permeability in unsaturated
54 conditions between a labcrete (concrete prepared and cured in the laboratory) and the
55 corresponding fieldcrete (same formulation of concrete prepared on a construction site); this is
56 obviously lacking in the scientific literature. The influence of the on-site cure (*e.g.* early-age
57 drying) and structural effects (*e.g.* cracking) is not addressed in this article and should be the
58 subject of a further study. Specifically, mass loss due to drying of several specimens from
59 saturation up to 30% of relative humidity is measured. The results are then used for identifying
60 by inverse analysis and comparing the parameters of a classical model describing the water
61 transfer via a single mass balance equation. Besides this experimental procedure, one-
62 dimensional numerical simulations are performed to analyze the sensitivity of the saturation
63 profiles towards the identified materials parameters. Further, 3D simulations on mesoscale
64 concrete specimens exhibiting different aggregate distributions are performed to investigate
65 more precisely local effects due to the presence of aggregates on the saturation degree.

66 2. Material and methods

67 2.1. Concrete

68 The concrete used in this study was designed by the Belgian agency for radioactive waste and
69 enriched fissile materials (ONDRAF-NIRAS¹) in the framework of a project of Low-Level
70 radioactive waste surface disposal in Dessel, Belgium (Ondraf-Niras, 2010). It is a modern
71 concrete including CEM I (Ordinary Portland Cement) with a water-to-cement ratio of 0.47. The
72 superplasticizer (Masterglenium® 27) content was adjusted so that the slump of the fresh mix
73 would reach 19 cm. The average compressive strength at 28 days is equal to 49 MPa using

¹ <http://www.nirond.be>

74 cylinders (68 MPa was obtained using cubes). A large experimental campaign was undertaken at
 75 the Eduardo Torroja Institute (IeTcc²) in which many characterization tests were conducted on a
 76 preliminary but very similar composition [31] along with a sensitivity analysis at the Belgian
 77 Building Research Institute [32], demonstrating its robustness. Among all of them the first
 78 desorption isotherm was acquired. This concrete (Table 1) was studied in laboratory and was
 79 also produced in industrial conditions for the realization of test panels (11 m height, 3 m long) to
 80 verify its feasibility for the construction of surface disposal modules in Dessel. Up to this day,
 81 three test panels have been erected with this composition, each of them containing about 25 m³
 82 concrete. About 6 to 10 batches were furnished during the construction of each test panel. The
 83 fieldcrete used in this study was produced during one of these test panels. **The cubes were**
 84 **fabricated on-site by the site workers. They were unmolded the day after casting and they were**
 85 **then kept in a humid chamber (RH>95%, ca. 20°C) for 28 days. After that, the specimens were**
 86 **kept under water at ambient temperature for multiple months before use.**

87 In the laboratory the concrete (labcrete) was mixed in small batches (30 L) and cylindrical
 88 specimens (Ø11×H22 cm) were prepared that were normally vibrated and then kept in their
 89 sealed molds before use.

90 *Table 1 – composition of the concrete*

Compound	Nature	Quantity (kg/m³)
Low-heat cement	CEM I 42.5 LH	360
Filler	Limestone (Calcitec)	40
Water		169
Gravel 6/20 mm	Limestone	472
Gravel 6/14 mm	Limestone	200
Gravel 2/6 mm	Limestone	417
Sand 0/4 mm	Limestone	721
Superplasticizer	Glenium 27 (BASF)	1.8 (0.5 wt% of cement)

91

² <http://www.ietcc.csic.es/index.php/en/>

92 2.2. Methods

93 Four mature labcrete specimens ($\emptyset 11 \times H 22$ cm), that were kept two years in their sealed molds
94 after casting, were cored to generate 4 smaller cylinders ($\emptyset 6 \times H 22$ cm). Top and bottom ends,
95 whose properties may differ from the bulk [33–36], were sawn and thrown away. This resulted
96 in four new cylinders ($\emptyset 6 \times H 15$ cm) that assumedly exhibited uniform properties. In the same
97 way, five mature fieldcrete cubes ($15 \times 15 \times 15$ cm), originating from five different batches, were
98 cored to generate two smaller cylinders ($\emptyset 6 \times H 15$ cm): 2 cylinders per cube. They were cut as
99 described above resulting in ten new cylinders ($\emptyset 6 \times H 11$ cm).

100 All the specimens were resaturated under water and vacuum [37] and the volume and density of
101 each specimen were measured using the buoyancy method (Table 2). All the saturated cylinders
102 were introduced in a climatic chamber at 25 °C and 55% RH for 230 days. The RH within the
103 chamber was then lowered to 30% for 105 more days. At given times, the chamber was opened
104 and the specimens' weight was measured to monitor their drying. Eventually, all the specimens
105 were completely dried at 105 °C for porosity evaluation.

106 2.3. Permeability assessment (inverse analysis)

107 The intrinsic permeability of the concrete was evaluated using inverse analysis [38–40]. Water
108 transport in unsaturated concrete was described making use of a simplified approach
109 accounting for liquid water permeation only. The contribution of other motions (gas phase
110 permeation and diffusion of vapor) was neglected [38]. Finally, the only differential equation to
111 solve was the following [41,42]:

$$\phi \left(\frac{\partial S}{\partial P} \right) \frac{\partial P}{\partial t} = \text{div} \left[\frac{K k_r}{\eta} \text{grad}(P) \right] \quad (1)$$

112 with:

- 113 • ϕ the concrete porosity (without unit)
- 114 • S the saturation degree of the porosity (without unit)
- 115 • P the water pressure within the pores (Pa)

- 116 • η the water viscosity (Pa s)
- 117 • K the intrinsic permeability (m²)
- 118 • k_r the relative permeability to water (without unit)

119 The equation proposed by van Genuchten [43] was used to describe the water retention curve:

$$S = \left[1 + \left(\frac{P}{P_0} \right)^{\frac{1}{1-m}} \right]^{-m} \quad (2)$$

120 where m and P_0 are two positive parameters that were identified using the experimental
 121 desorption isotherm measured at 20°C at IETcc [31]. The following resulting values were
 122 obtained: $m = 0.532$ and $P_0 = 59.05$ MPa. **It must be mentioned that the fieldcrete desorption**
 123 **isotherm was not measured and that a unique dataset was considered here: i.e. the desorption**
 124 **isotherm was assumed to be the same for the labcrete and for the fieldcrete. Fieldcretes are**
 125 **known to present more variability than labcretes [44]. Using fieldcrete specimens from different**
 126 **batches was then expected to possibly induce modifications in their desorption isotherm**
 127 **[44,45]. It should also be quoted that using different isotherm data for the labcrete and the**
 128 **fieldcrete might have yielded (slightly) different results in permeability [42]; however,**
 129 **considering variable isotherm curves was deemed unreasonable due to the number of tests that**
 130 **should have been conducted to characterize the desorption isotherm of all the specimens and**
 131 **the considerable time that would have been required.**

132 Following the proposition of Savage and Janssen [46], Mualem's model [43,47] was used to
 133 assess the relative permeability to water k_r :

$$k_r = \left[1 + \left(\frac{P}{P_0} \right)^{\frac{1}{1-m}} \right]^{-m\alpha} \left\{ 1 - \left(\frac{P}{P_0} \right)^{-\frac{m}{1-m}} \left[1 + \left(\frac{P}{P_0} \right)^{\frac{1}{1-m}} \right]^{-m} \right\}^2 \quad (3)$$

134 where α is the pore-interaction factor. It is a lumped parameter that accounts for the
 135 connectivity and tortuosity of the pore network. Mualem [47] suggested to use $\alpha = +0.5$ as
 136 default value and so it has been extensively used so far. It was however shown that using

137 $\alpha = +0.5$ could sometimes result in unacceptable fits [48] and that α could exhibit very different
138 values either positive or negative [49,50].

139 The left-hand term of eq. (1) was easily obtained by derivation of eq. (2):

$$\phi \left(\frac{\partial S}{\partial P} \right) = - \frac{m\phi}{(m-1)P_0} \left(\frac{P}{P_0} \right)^{\frac{m}{1-m}} \left[1 + \left(\frac{P}{P_0} \right)^{\frac{1}{1-m}} \right]^{-1-m} \quad (4)$$

140 In practice, eq. (1) was solved using the finite-element method and the code Cast3m³. In
141 accordance with the symmetry of the problem, the mesh only accounted for a sample quarter in
142 axisymmetric conditions (Figure 1): 75×150 four-node quadrangles were used in a non-uniform
143 grid. The initial conditions were uniform temperature $T_0 = 298.15$ K (25 °C) and water pressure
144 $P_0 = 0.0$ MPa (the samples were initially saturated). The boundary conditions were (for time $t \geq$
145 0): $T = 298.15$ K and $P = -82.1$ MPa for the 230 first days (55% RH) and then $P = -165.3$ MPa for
146 the rest of the simulation (30% RH). Please note that Kelvin's equation (5) was used to calculate
147 the water pressure P generated by the relative humidity h :

$$P = \rho \frac{RT_0}{M} \ln(h) \quad (5)$$

148 with:

- 149 • R the universal gas constant (8.3145 J/mol/K)
- 150 • ρ and M the water density (997.1 kg/m³) and molar mass (0.018 kg/mol) respectively

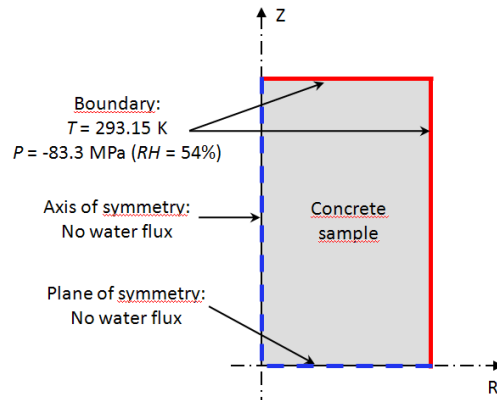
151 The intrinsic permeability K was then evaluated through the minimization of the quadratic
152 difference between the computed and measured mass variations:

$$F = \sum_{j=1}^N \left[\left(\frac{\Delta m}{m} \right)_j^{exp} - \left(\frac{\Delta m}{m} \right)_j^{sim} \right]^2 \quad (6)$$

153 with:

³ <http://www-cast3m.cea.fr/>

- 154 • N the number of mass measurements during the drying test (23 in our case: 12 at 55%
- 155 RH and 11 at 30% RH, see Figure 2)
- 156 • $\left(\frac{\Delta m}{m}\right)_j^{exp}$ and $\left(\frac{\Delta m}{m}\right)_j^{sim}$ the experimental and simulated mass loss for the measurement j ,
- 157 see eq. (7)



158 Figure 1 – schematic description of the mesh and boundary conditions

159

160 3. Results

161 3.1. Density and porosity

162 Table 2 presents the density and porosity results. It is interesting to note that the porosity of the

163 fieldcrete (11.9%) was greater than that of the labcrete (10.6%). This was consistent with the

164 density results: the density of the fieldcrete (2.432) was found to be lower than that of the

165 labcrete (2.472). Moreover the intrinsic permeability of the fieldcrete was always greater than

166 that of the labcrete, irrespective of the RH-step, and the experimental scatter obtained for the

167 fieldcrete is about seven times greater than that of the labcrete. This was believed to be due to

168 the increased difficulty of the concreting operations on site as well as to the five different

169 batches [44].

170

171

Table 2 – density and porosity of the concrete specimens

Concrete	Batch	Specimen	Density		Porosity	
			Individual value	Average (COV)	Individual value	Average (COV)
Labcrete	1	I	2.474	2.472 (0.1%)	10.6%	10.6% (0.8%)
		II	2.469		10.7%	
		III	2.471		10.7%	
		IV	2.472		10.6%	
Fieldcrete	1	1-1	2.421	2.432 (0.6%)	12.1%	11.9% (6.5%)
		1-2	2.455		11.6%	
	2	2-1	2.440		11.6%	
		2-2	2.439		12.0%	
	3	3-1	2.439		11.6%	
		3-2	2.404		12.3%	
	4	4-1	2.440		11.8%	
		4-2	2.444		11.6%	
	5	5-1	2.419		12.4%	
		5-2	2.417		12.2%	

173

174 3.2. Isothermal drying test

175 Figure 2 presents the variations of the specimens' mass loss versus time all along the drying
 176 experiment. The experimental mass loss $\left(\frac{\Delta m}{m}\right)$ was calculated for each specimen as follows:

$$\left(\frac{\Delta m}{m}\right)(t) = \frac{m(0) - m(t)}{m(0)} \quad (7)$$

177 where $m(0)$ and $m(t)$ are the initial mass of the specimen and the mass at time t respectively.

178 It is interesting to note that the fieldcrete behaved differently compared to the labcrete: the
 179 mass loss was always significantly greater (in line with the porosity that was higher) as well as
 180 the discrepancy. Here again, the five different batches as well as the difficulty of the concreting
 181 operations onsite may be held responsible.

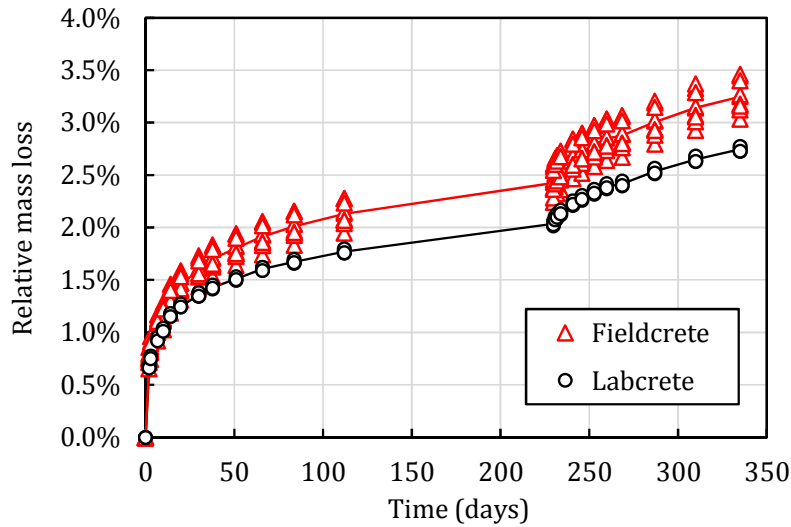


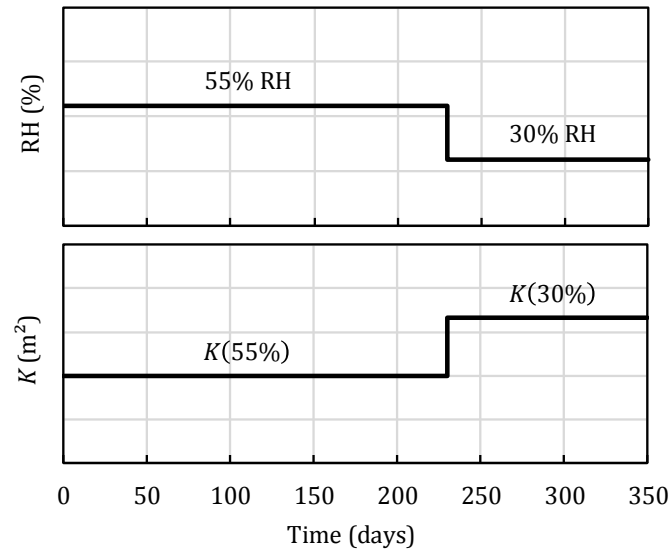
Figure 2 – mass loss variation versus time

182

183

184 3.3. Permeability assessment

185 In a first step, the intrinsic permeability was evaluated using inverse analysis independently on
 186 the two RH steps (55% and then 30%). The process detailed in section 2.3 was applied to all the
 187 specimens. Following Mualem’s suggestion [47] and without relevant information about its
 188 value, the pore-interaction factor α was taken equal to +0.5 (1st run, Table 3). Separate
 189 simulations were conducted for each specimen considering individual data, namely density,
 190 porosity and mass loss (Table 2). The permeability assessment was done in two consecutive
 191 steps. Firstly, the process detailed in section 2.3 was used to assess the permeability of all the
 192 specimens using the results of the first drying phase only (55% RH). In a second step, the results
 193 of the second drying phase (30% RH) were used in the same way to assess the permeability of
 194 all the specimens once again. In that case, the permeability was assumed to be a piecewise
 195 function of time (cf. Figure 3): during the first 230 days (first drying phase at 55% RH) the
 196 permeability was fixed to the value obtained in the first simulation and after that the
 197 permeability value was adjusted to reproduce the experimental mass variations during the
 198 second drying phase (30% RH).



199

200

Figure 3 – RH and permeability for the 1st run of drying simulations

201

202 This approach yielded two different intrinsic permeability values for each specimen: $K(55\%)$

203 and $K(30\%)$ that are presented on Figure 4. The variability obtained for the fieldcrete was

204 always significantly greater than that of the labcrete (about 4 times) in accordance with the

205 experimental mass loss results (Figure 2).

206

Table 3 - summary of the simulations

Parameters/properties		1 st run	2 nd run
Porosity	\emptyset	See the individual values of	See the individual values of
Density	d_s	Table 2	Table 2
van Genuchten exponent	m	0.532	0.532
van Genuchten pressure	P_0	59.05 MPa	59.05 MPa
Pore interaction factor	α	+0.5	α and K adjusted together
Intrinsic permeability	K	adjusted on the two RH steps (30% & 55%) resulting in two distinct values	using the results of the two RH steps (30% & 55%) resulting in a unique dataset

207

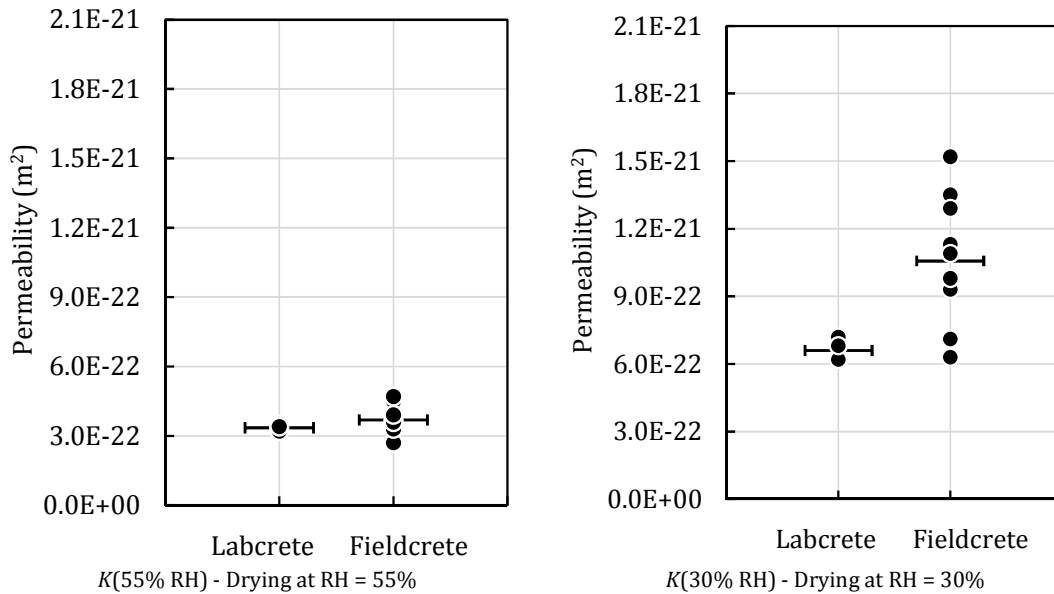
208 It is noteworthy that the intrinsic permeability values obtained at 30% RH were higher than

209 those of 55% RH (by a factor 2-3, see 1st run in Table 4). This indicated that the relative

210 permeability k_r was not correctly estimated and more specifically the slope between 55% and

211 30% RH was overestimated. This was due to the choice of the α value (+0.5) that did not

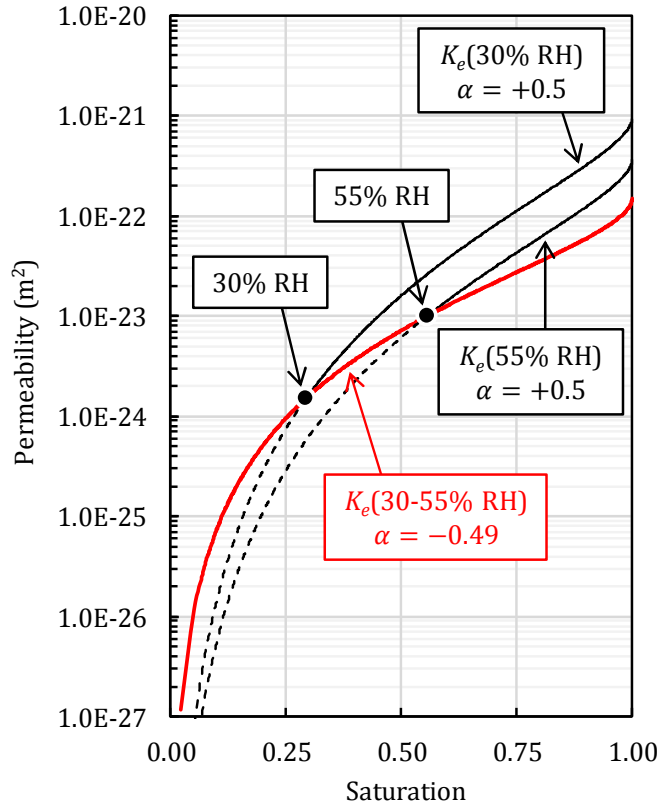
212 properly describe the relative permeability variations of the considered concrete. This is known
 213 to induce significant discrepancy in the assessment of the intrinsic permeability over different
 214 RH ranges [41].



215

Figure 4 - intrinsic permeability assessment using $\alpha = +0.5$

216 In a second step, the pore interaction factor α was considered as an unknown empirical
 217 parameter that needed to be calibrated together with the intrinsic permeability K as it is
 218 commonly done in soil science [48–53] (2nd run, Table 3). The value of α was adjusted so that the
 219 effective permeability (*i.e.* the product $K \times k_r$) matched the two different effective
 220 permeabilities assessed at 55% and 30% RH (see the two black spots on Figure 5). The α -values
 221 thus obtained are reported in Table 4 (column ‘2nd run’). In so doing, it was believed that the
 222 slope of the effective permeability curve was correctly calibrated (at least between 55% and
 223 30% RH).



224

225

Figure 5 – calibration of the pore-interaction factor α (example of the fieldcrete specimen 1-1)

226

New simulations of the drying experiments were conducted for all the concrete specimens using

227

the pore interaction factor values that were obtained above. For each specimen a unique value of

228

intrinsic permeability was identified that made it possible to describe the mass loss variation all

229

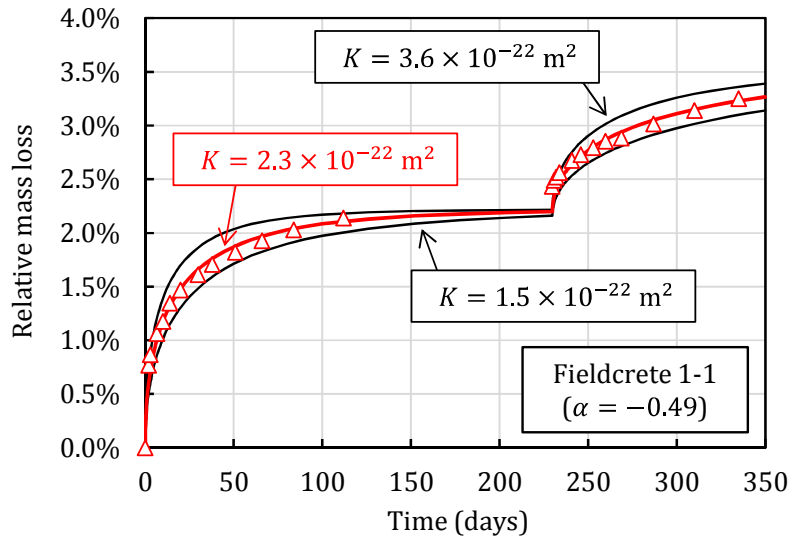
along the drying experiment (see 2nd run in Figure 6). This proved that the pore interaction

230

factor α was properly evaluated and that the resulting data set could be used to describe

231

accurately the water exchange with the environment down to 30% RH.



232

233 *Figure 6 - new assessment of the intrinsic permeability K using $\alpha \neq +0.5$ (example of the fieldcrete specimen*
 234 *1-1)*

235 All the results in terms of permeability and pore interaction factor are reported in Table 4 and
 236 plotted in Figure 7. It is interesting to note that after the second assessment step, the intrinsic
 237 permeability values obtained for the fieldcrete were very close to those of the labcrete (Figure
 238 8). This was not the case after the first step. Reevaluating the pore interaction then helped to
 239 improve the accuracy of the evaluation and eventually show that the labcrete and fieldcrete
 240 were very similar in terms of intrinsic permeability ($2 \times 10^{-22} \text{ m}^2$). The reader must keep in mind
 241 though that the intrinsic permeability assessed using inverse analysis depends on the model and
 242 input data used [42]. One can wonder whether the conclusion would have been the same using a
 243 different evaluation process.

244 All the pore interaction factors presented negative values that were different for the labcrete
 245 and fieldcrete: they ranged between -0.5 to -0.6 for the labcrete and between -1.0 to -1.4 for the
 246 fieldcrete. It is noteworthy that all these values were different from the value suggested by
 247 Mualem (+0.5). This has been known for long for soils for which many results were published
 248 [47–50,53–55]. In the field of cement-based materials, results are scarce. A positive value of +5.5
 249 was proposed using gas permeability tests [2,56] but negative values were obtained by Leech et
 250 al. [57] using capillary absorption tests: they obtained values ranging from -0.2 to -1.2. Later

251 Poyet *et al.* [41] dried partially carbonated specimens with decreasing RH steps and after
 252 inverse analysis obtained values ranging from -1.5 to -4.0. It is interesting to note that the values
 253 obtained in this study for the labcrete matched the proposition of Leech *et al.* to use $\alpha = -0.5$
 254 instead of +0.5 [57]. The α -values of the fieldcrete were somewhat lower (-1.2 in average).
 255 In terms of experimental scatter, the variability of the intrinsic permeability of the labcrete was
 256 very low: the coefficient of variation was 3%. This was expected because all the four specimens
 257 were carefully fabricated in the laboratory using the same concrete batch. The coefficient of
 258 variation of the fieldcrete was found to be higher (12%) because the specimens originated from
 259 five different concrete batches that were fabricated onsite by the workers in charge of the
 260 realization of the surface disposal mockup. The coefficient of variation that was found for the
 261 fieldcrete however remained limited compared to the values obtained in other studies – see for
 262 instance [44] - indicating that it is possible to limit the variability of concretes *in situ*.

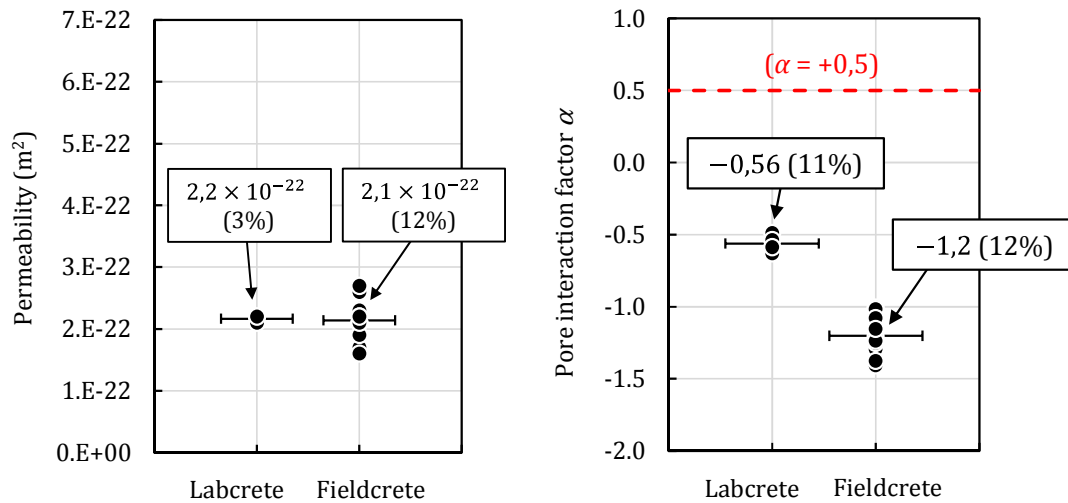
263

264

Table 4 – intrinsic permeability and pore interaction factor data

Concrete	Batch	Specimen	1 st run			2 nd run	
			α	$K(55\% \text{ RH})$	$K(30\% \text{ RH})$	α	K
Labcrete	1	I	+0.5	3.3×10^{-22}	6.2×10^{-22}	-0.49	2.2×10^{-22}
		II	+0.5	3.2×10^{-22}	6.2×10^{-22}	-0.54	2.1×10^{-22}
		III	+0.5	3.5×10^{-22}	7.2×10^{-22}	-0.63	2.2×10^{-22}
		IV	+0.5	3.4×10^{-22}	6.8×10^{-22}	-0.59	2.2×10^{-22}
Fieldcrete	1	1-1	+0.5	3.6×10^{-22}	9.4×10^{-22}	-1.00	2.3×10^{-22}
		1-2	+0.5	2.7×10^{-22}	7.1×10^{-22}	-1.02	1.7×10^{-22}
	2	2-1	+0.5	3.5×10^{-22}	11.0×10^{-22}	-1.30	1.6×10^{-22}
		2-2	+0.5	3.7×10^{-22}	11.3×10^{-22}	-1.25	2.2×10^{-22}
	3	3-1	+0.5	3.4×10^{-22}	9.3×10^{-22}	-1.08	2.1×10^{-22}
		3-2	+0.5	4.5×10^{-22}	15.2×10^{-22}	-1.41	2.6×10^{-22}
	4	4-1	+0.5	3.3×10^{-22}	9.8×10^{-22}	-1.21	1.9×10^{-22}
		4-2	+0.5	3.6×10^{-22}	10.9×10^{-22}	-1.24	2.1×10^{-22}
	5	5-1	+0.5	4.7×10^{-22}	13.5×10^{-22}	-1.15	2.7×10^{-22}
		5-2	+0.5	3.9×10^{-22}	12.9×10^{-22}	-1.38	2.2×10^{-22}

265



266 Figure 7 – intrinsic permeability K (left) and pore interaction factor α (right) of the concrete specimens

267 Figure 8(a) compares the unsaturated permeability evolutions for all the tested specimens.

268 Although the intrinsic permeability values ($S=1$) were more or less the same for the labcrete and

269 the fieldcrete, the fieldcrete specimens were always more permeable than the labcrete ones. At

270 55% RH ($S=0.555$), the effective permeability of the fieldcrete was between once and twice that

271 of the labcrete. At 30% RH ($S=0.293$), the effective permeability of the fieldcrete was between

272 1.4 and 3.4 times that of the labcrete (Figure 8(b)). This was due to the differences in pore-

273 interaction factor α (Figure 7) that influenced the slope of the effective permeability. **It is**

274 **noticeable that, below 30% RH, the fieldcrete permeability steeply increased faster than that of**

275 **the labcrete when saturation decreased. The fieldcrete permeability could then be ten times**

276 **higher than that of the labcrete for very low saturation values. However this point was not**

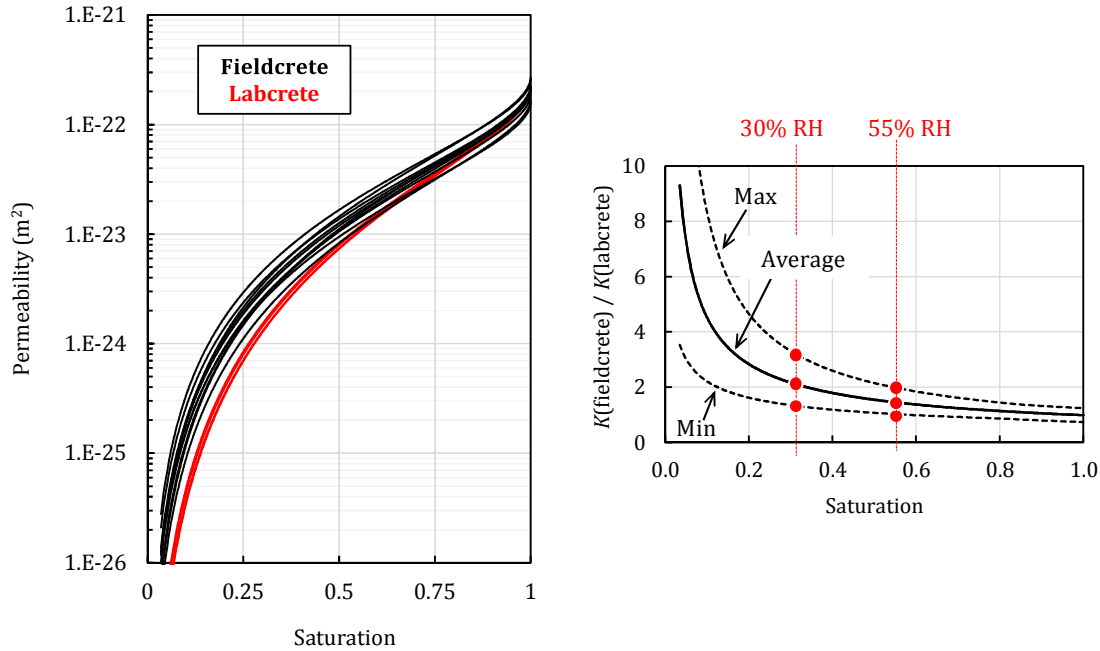
277 **judged significant for two reasons. Firstly, it must be recalled that this increase was obtained for**

278 **RH values that were much lower than 30%; these values are almost never encountered in real**

279 **life. Secondly, the increase was obtained for saturation values that were very far from the RH-**

280 **domain in which the permeability was evaluated. This increase might then be somewhat**

281 **questionable.**



(a) unsaturated permeability evolution of all the tested specimens (b) ratio of the fieldcrete permeability to that of the labcrete

Figure 8 – unsaturated permeability evolutions for all the labcrete (in red) and fieldcrete (in black)

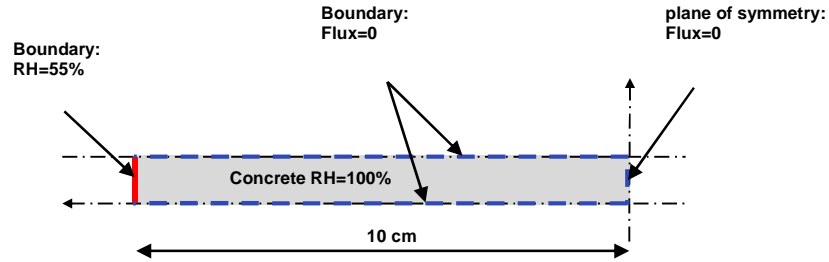
specimens

4. Application: simulations of drying

4.1. 1D simulation of a homogeneous material

To illustrate the effects of the identification procedure on the saturation degree profiles, we propose to simulate in this section the case of a homogeneous material subjected to drying at constant relative humidity. The parameters identified in the previous section will be successively adopted and the obtained results will be compared. The structure considered consists of a fraction of concrete wall with thickness 20 cm, and with its two opposite faces exposed to a relative humidity of 55% (see Figure 9). The drying phenomenon is assumed to occur perpendicularly to these faces and is one-dimensional, though the resolution of the problem is 2D. **For symmetry reason, only half of the structure is considered.** Again, the finite element code Cast3m is used to solve eq. (1), with 400 elements having variable dimensions (their size is smaller near the exposed surface to capture accurately the high gradients appearing when the loading is applied, and increases progressively) to discretize the structure.

297

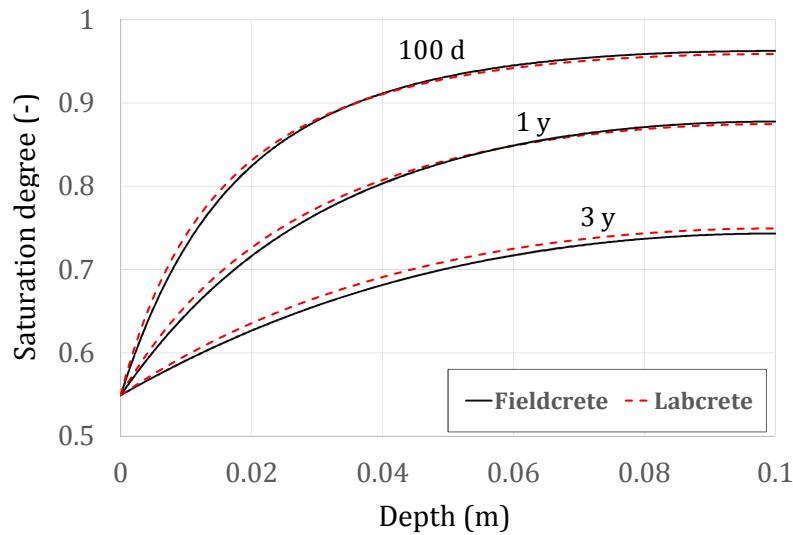


298

299

Figure 9 – schematic description of the 1D simulations and boundary conditions

300 The first simulation is intended to compare the results of labcrete and fieldcrete corresponding
 301 to the identification procedure with $\alpha \neq 0.5$ shown in Figure 7, *i.e.* for the mean values of
 302 parameters for both materials. Note that the respective average value of porosity (see Table 2) is
 303 used for each case. The saturation degree profiles obtained at 100 days, 1 year and 3 years of
 304 drying are plotted in Figure 10 as a function of the depth, $x=0$ designating the exposed face. Very
 305 few differences can be observed between labcrete and fieldcrete profiles, indicating that on
 306 average the two materials exhibit similar drying processes and then close permeability
 307 properties in unsaturated conditions.



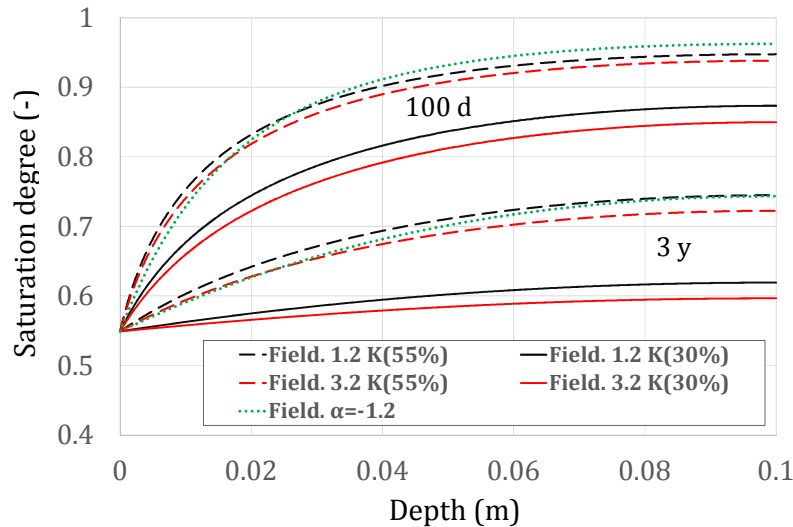
308

309

310 *Figure 10 – saturation profiles at 100 days, 1 year and 3 years for labcrete and fieldcrete obtained with the*
 311 *parameters of Figure 7*

312 We now examine the influence of the permeability value retained for the identification (*i.e.*, at 30
 313 and 55% HR, see Figure 5 and Table 4, 1st run) on the description of the drying kinetics when the

314 parameter α is kept equal to 0.5. Figure 11 presents the saturation profiles obtained at 100 days
 315 and 3 years in the case of fieldcrete 1.2 and 3.2, and for the two values $K(55\%)$ and $K(30\%)$.
 316 These cases are chosen because they appear to envelop all curves with the $\alpha = -1.2$
 317 identification procedure (see Figure 12). For the sake of comparison, we also reported in dotted
 318 lines the curves simulated with $\alpha = -1.2$ and shown on Figure 10.



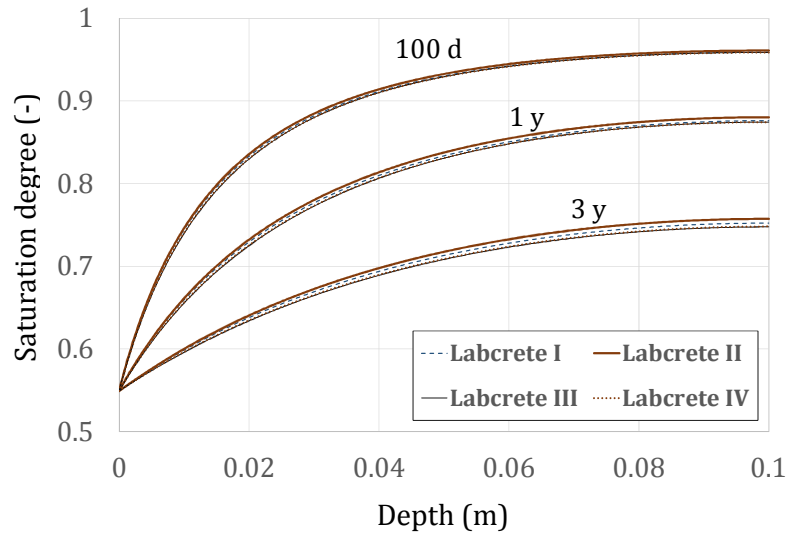
319
 320

321 *Figure 11 – saturation profiles at 100 days and 3 years for fieldcrete 1.2 and 3.2 obtained with parameters*
 322 *$\alpha = 0.5$ and two values of permeability; comparison with the identification of Figure 7 ($\alpha = -1.2$)*

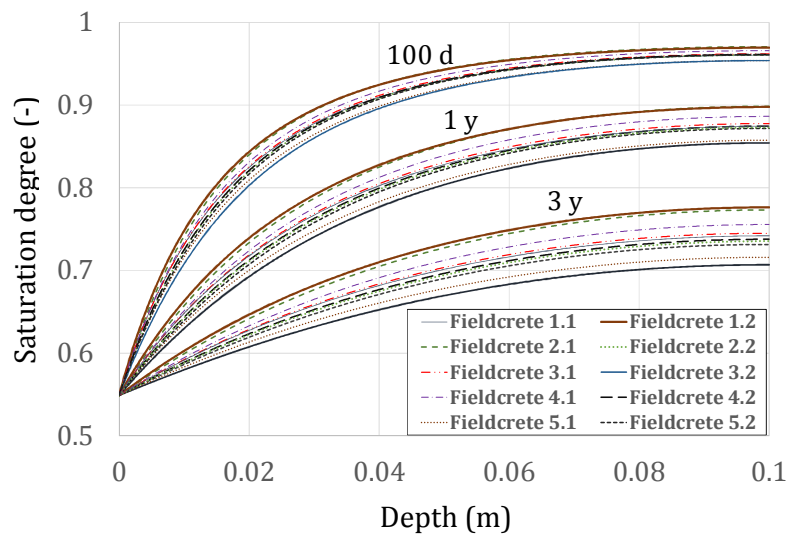
323 We first observe that the saturation profiles simulated with the two permeability values exhibit
 324 very significant differences. Further, the $K(55\%)$ curves are at the same time close to each other
 325 and close to the $\alpha = -1.2$ average case. This is not very surprising since the validity domain of
 326 the parameters identified at 55% is more consistent with the practical RH domain covered in the
 327 simulation than the one identified at 30%. Finally, we conclude that the $K(55\%)$ with $\alpha = 0.5$
 328 values provide saturation profiles in good concordance with those obtained with the $\alpha = -1.2$
 329 identification method.

330 Figure 12 presents the saturation profiles obtained at 100 days, 1 year and 3 years for all
 331 labcrete (top) and fieldcrete (bottom) specimens calculated with the parameters of the 2nd run of
 332 Table 4 corresponding to $\alpha \neq 0.5$. We observe that for labcrete, the curves are relatively close
 333 whatever the samples considered, while for fieldcrete the scatter is as expected much more

334 significant. Although we may argue that the greater number of fieldcrete specimens also
 335 contributes to this larger variability, the more disperse response for these concrete samples
 336 appears clearly and leads to important differences in saturation profiles.



337
 338



339
 340

341 *Figure 12 – saturation profiles at 100 days, 1 year and 3 years for all labcrete (top) and fieldcrete (bottom)*
 342 *specimens calculated with the parameters of the 2nd run of Table 4*

343

344 These results are totally in line with those shown on Figure 2 and Figure 8. The discrepancies in
 345 the saturation degree profiles increase as a function of time (at least up to 3 years), which means
 346 that the time needed for obtaining a quasi-homogeneous saturation profile may differ

347 considerably in particular between the fieldcrete specimens. As a corollary, the question of the
348 notion of representative elementary volume is posed as it may not to be the same for labcrete
349 and fieldcrete, *i.e.* a greater volume is expected for fieldcrete to appropriately represent the
350 material with a variability similar to the labcrete one.

351 Among the possible causes of the greater variability in the fieldcrete results, a more significant
352 dispersion in the spatial repartition of the different components (aggregates, cement paste,
353 pores) due to a lower homogeneity in the casting procedure, and the variability in the actual
354 formulation, are expected to be of importance. We propose to examine the first aspect in the
355 next section through simulations of mesoscale concrete specimens exhibiting a different
356 aggregate distribution.

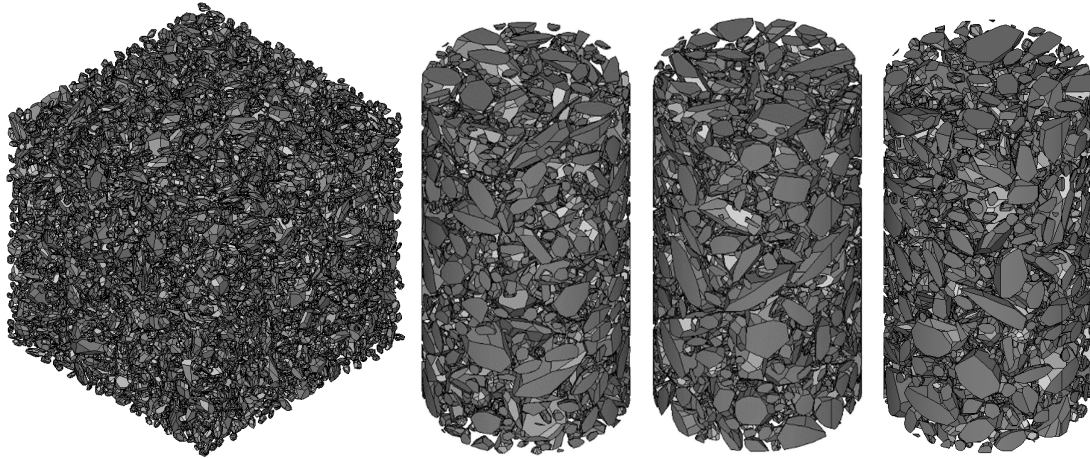
357

358 4.2. Simulation of 3D concrete samples

359 To investigate the role of the aggregates within the specimens on the overall drying kinetics, we
360 propose to perform mesoscale 3D simulations on numerical samples generated with different
361 aggregate distributions and shapes. Such mesoscale simulations on concrete representative
362 volumes involving explicitly the aggregates are increasingly used due to the growing power of
363 computers to analyze various effects and characterize properties related to (possibly coupled)
364 mechanical, diffusive and chemical problems, see for instance [58–61] In this paper, to be as
365 close as possible to the experimental conditions of fieldcrete testing, the numerical samples are
366 constructed following the experimental procedure, *i.e.* cubic concrete volumes with dimensions
367 15×15×15 cm are generated, from which cylindrical samples of diameter 6 cm and height 11 cm
368 are extracted (cored). The aggregate dimensions are imposed by the actual grading curve. Note
369 that the aggregates are generated numerically with convex polyhedral shapes obtained by a
370 Voronoi space decomposition, which is a notable difference with *e.g.* [61] in which aggregates
371 are spherical. The aggregates are next modified to conform to a prescribed aspect ratio
372 randomly chosen between 1 and 4 along two perpendicular directions, so as to generate

373 flattened/elongated shapes. The numerical procedure makes use of the functionalities of the
374 CAD code Salome (www.salome-platform.org), and is described in more details in *e.g.* [62–64].
375 Although these numerical aggregates are expected to be relatively realistic, the obtained
376 approximated shapes (in particular, real aggregates are not in general convex) may introduce a
377 certain bias in the results. However it has been reported in [65] that regarding viscoplastic
378 mechanical behavior, such numerical aggregates reproduce relatively well the overall concrete
379 behavior when compared to real aggregates obtained by tomography. A similar study regarding
380 transport properties would be necessary to investigate the impact of real versus numerical
381 aggregates.

382 Figure 13 left presents a generated cubic specimen with 12370 aggregates (left), corresponding
383 to an aggregate volume fraction of 35% and a minimum size on the grading curve of 3.6 mm.
384 Such ratio is deemed to be sufficiently realistic to achieve representative results, while keeping
385 the computation costs reasonable. Note that the random process of particle placing accounts for
386 a minimum distance between aggregates, and has to fulfill the non-overlapping condition with
387 the cube surfaces. Figure 13 right shows the aggregate distribution in 3 cylindrical specimens
388 cored from different cubic samples. For the simulations, 6 samples have been extracted from 3
389 different cubes. Interestingly, the aggregate volume fraction calculated in the specimens ranges
390 between 0.374 and 0.383, which is significantly higher than the one imposed in the initial cubic
391 volumes due to the wall-effect and corresponding non-homogeneity of the aggregates
392 repartition in the cubes between regions near the surfaces and the core.



393

394

Figure 13 – example of $15 \times 15 \times 15$ cubic specimen generated with 12370 aggregates (left); aggregate

395

distribution in 3 cylindrical specimens constructed from the cubic samples (right)

396

The meshes are generated automatically by the meshing softwares MG-CADSurf and MG-Tetra

397

developed by Distene⁴, and plugged in Salome. The total number of tetrahedral elements in the

398

meshes of the cylindrical specimens range between 2.26 and 2.32×10^6 . The simulations consist

399

of a drying test from an initial totally saturated state during 1 year, and with the lateral surfaces

400

of the specimens exposed to an environment with $RH = 0.55$. To focus on the aggregate shape

401

effects and ease the comparison, the material parameters of the matrix phase (corresponding

402

here to the mortar) are supposed to be the same for all samples, and are taken as $K = 2 \times 10^{-22} \text{ m}^2$,

403

$\alpha = -0.56$, and $\phi = 0.2$. **Note that as the values of K and α are not identified experimentally on**

404

mortars, they are simply set from those determined for concretes in the previous sections, given

405

that we do not expect that the results regarding the effects of aggregate shapes would be

406

different with (slightly) altered values. The macroscopic transport properties obtained on the

407

numerical specimens with these values for mortar are calculated and discussed in the sequel.

408

The aggregates are not accounted for in the calculations since they are supposed to be non-

409

diffusive. Also, the possible preferential pathways for transport at the interfaces between

410

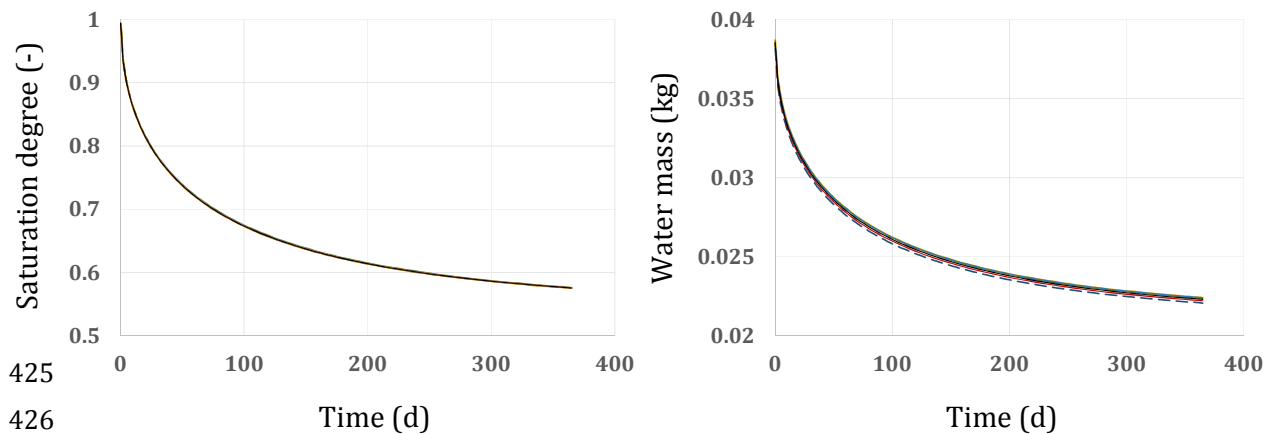
aggregates and matrix (the so-called ITZ) are ignored here. Indeed, we assume that, as by

⁴ <http://www.distene.com>

411 construction these interfaces do not form a connected network, their impact on the overall
412 results is weak.

413 Figure 14 presents the simulation results in terms of time evolution of overall saturation degree
414 (left) and water mass (right) calculated within all 6 specimens. The mass of water is simply
415 obtained from the saturation degree and the average porosity in the whole samples, *i.e.* the
416 porosity corrected by the volume fraction of matrix. We can observe that the saturation degree
417 curves are identical for all cases, while the water mass ones exhibit a slight difference. The latter
418 are mainly attributed to the different mean porosity in the samples, which is a consequence of
419 the variable volume fraction of matrix due to the random generation process of the numerical
420 samples. From these results, we may assert that, on average, the global drying response is nearly
421 the same for the specimens. This indicates that regarding the saturation degree averaged over
422 the entire volume, the influence of the aggregate distribution as investigated in this section is
423 negligible.

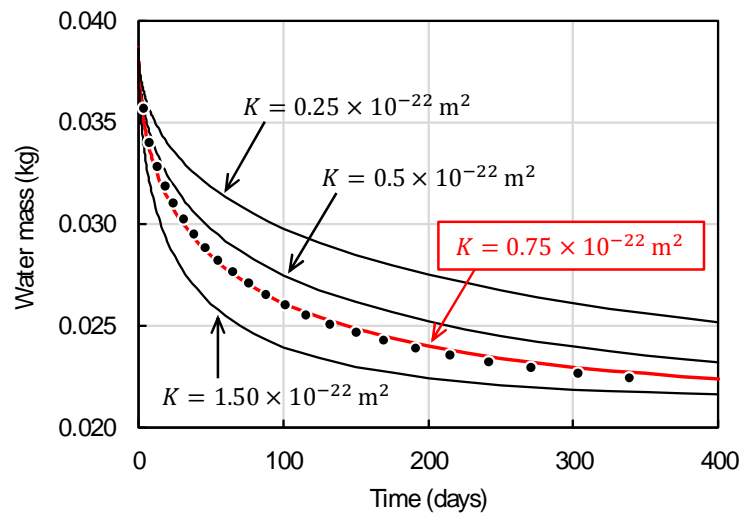
424



427 *Figure 14 – evolution of the overall saturation degree (left) and mass of water (right) for the 6 calculated*
428 *specimens*

429 As mentioned above, it may be instructive to characterize the macroscopic (or equivalent)
430 transport parameters of the generated numerical concretes, from the results of water mass loss
431 of Figure 14 as done in section 3 from experiments, and to compare them with the input data of
432 mortar. Assuming the same value of α for both materials, *i.e.* $\alpha = -0.56$, we then propose to

433 apply the inverse analysis procedure described above to identify the permeability coefficient.
 434 Figure 15 presents the curves obtained on a homogeneous cylinder of diameter 6 cm and height
 435 11 cm with different values of K (continuous lines), and the mean curve resulting from the 3D
 436 numerical simulations on the 6 reconstructed specimens (points). The comparison indicates that
 437 the value $K=0.75 \times 10^{-22} \text{ m}^2$ leads to a water mass loss kinetics very close to the numerical
 438 concrete one. This means that the hypothesis on the value of $\alpha = -0.56$ is relevant for the
 439 homogenous material; on the other hand, the permeability coefficient K is significantly lower
 440 than the one of the mortar.



441

442 *Figure 15 – evaluation of the average permeability of the 6 reconstructed 3D specimens using inverse*
 443 *analysis (they were considered as homogeneous materials)*

444

445 It is important to notice that while the identification procedure is performed on a material
 446 assumed as homogeneous, hence with its entire boundary surfaces exposed to drying, the
 447 exchange of water takes place only through the contact surfaces between mortar and
 448 atmosphere in the 3D simulations, since the aggregates that overlap the lateral surfaces are non-
 449 diffusive. This means that the surface exposed to drying is much lower in the latter case than in
 450 the former one, which may according to the authors explain at least partly the important
 451 difference between macroscopically identified permeability coefficient and the prescribed input

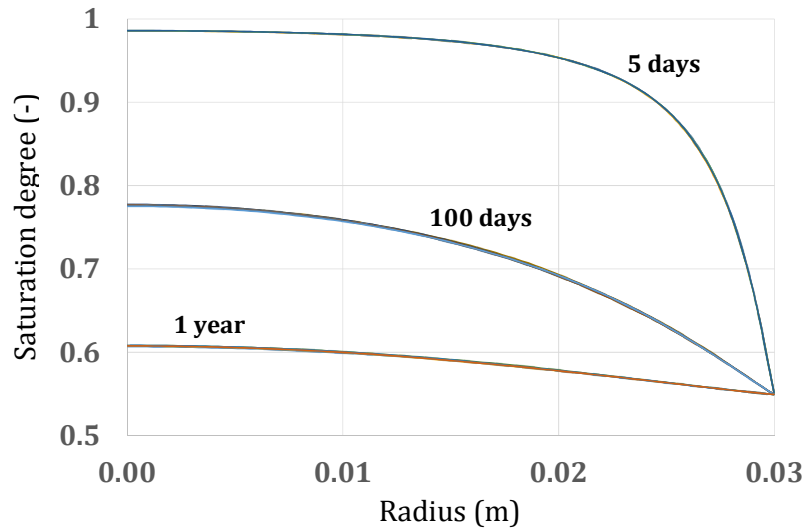
452 data set for the mortar. Indeed, it is doubtful that that the dilution effect and tortuosity due to
453 the presence of aggregates, which represent about 40% of the volume in the generated
454 specimens, may be totally responsible for a permeability coefficient decrease by a factor of 2.7.
455 To be more directly comparable, the value for mortar should also be affected by the reduction of
456 drying surface. As a first approximation, if we simply consider the same ratio for the surface
457 available for exchange and the volume fraction of mortar in concrete, *i.e.* around 60%, and that
458 this ratio may be directly applied for estimating the 'homogenized' mortar permeability in the
459 homogenous concrete, we arrive at a value of $K \approx 1.2 \times 10^{-22} \text{ m}^2$ instead of $K = 2 \times 10^{-22} \text{ m}^2$, which
460 seems in better agreement with the macroscopic value of $0.75 \times 10^{-22} \text{ m}^2$. This aspect would
461 however deserve further investigation.

462 To investigate in more details the numerical results on the 3D specimens, Figure 16 shows the
463 saturation degree profiles in the 6 samples at 5 days, 100 days and 1 year. The horizontal axis
464 designates the radius of the specimens, with 0 being the center and 0.03 the external surface.
465 The curves are obtained by averaging the calculated saturation degree fields on cylindrical
466 surfaces whose axis is identical to the samples one and whose radius evolves progressively from
467 0 to 0.03. Compared to Figure 14 showing volume-averaged quantities, Figure 16 then presents
468 surface-averaged results, which are deemed to provide more insightful and accurate information
469 about the aggregate distribution effects. We observe however that the curves for the different
470 specimens cannot be really distinguished; only a very small discrepancy may be seen on the 100
471 days results. This means that, in line with the conclusion on Figure 14, the saturation degree
472 profiles are not significantly affected by the aggregate distribution as considered here.

473 Finally, Figure 17 presents the numerical results in a more local manner than the two previous
474 Figures, with the saturation degree averaged over circles centered on the specimen axis. The
475 procedure is basically similar to the one leading to Figure 16, except that the cylindrical surfaces
476 of interest are here sampled by plans perpendicular to the axis. The idea is to examine the
477 evolution of the saturation degree along the axial direction at prescribed distances from the

478 surface exposed to drying, and at different times. We propose to analyze the results near the
479 lateral surface at the radius $r = 0.027$ m, and also at mid-distance between the axis and the
480 surface at the radius $r = 0.015$ m, corresponding to Figure 17 top and bottom, respectively, and
481 at 5, 25 and 100 days. The abscissa designates the position of the points along the axis, with 0
482 being arbitrarily the lower cross-section of the specimens. We observe that the results at
483 $r = 0.027$ (top) exhibit non-negligible variations along the axis direction, but also between the
484 different specimens. This is particularly visible at the onset of drying (5 days), while the curves
485 tend progressively to homogenize at greater times, with differences becoming relatively weak at
486 100 days. Maximum discrepancies of about 4.5% and 2.5% are reported at 5 days and 100 days,
487 respectively. The results at $r = 0.015$ show an opposite tendency: from the initial prescribed
488 homogeneous state, the saturation degree turns out to gradually disperse for increasing times,
489 though moderately; at 100 days, the maximum difference between all results is less than 3%.

490 To sum up, the curves of Figure 17 indicate that the aggregates influence locally the drying
491 phenomenon all the more that the gradients of saturation degree (or equivalently of capillary
492 pressure) are high, *i.e.* the kinetics of transport is rapid. At the beginning of the simulations these
493 gradient are maximal near the exposed surfaces, and the presence of aggregates as obstacles to
494 water transfer is noticeable. By contrast, when gradients are low as in the specimen centers or at
495 greater times, their influence and correspondingly their size and shape distribution, become
496 more and more negligible.

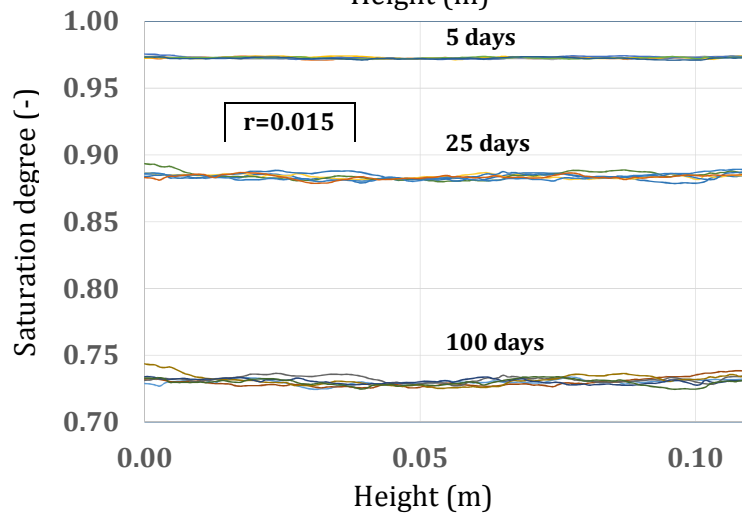
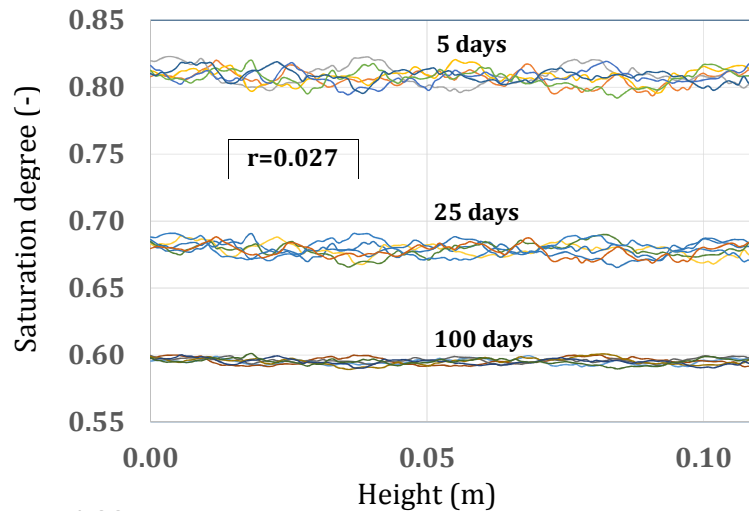


497

498

499 *Figure 16 – saturation degree profiles as a function of the radius for the 6 calculated specimens at 3 different*
 500 *times*

501 To conclude with the 3D numerical simulations presented in this subsection, the spatial
 502 distribution of aggregates within the samples seem to have a limited impact on the drying
 503 characteristics. When examining saturation degree evolutions as volume- and surface- averaged
 504 quantities, this aspect is clearly negligible. Locally, the influence of aggregates is visible in the
 505 zones where the gradients of capillary pressures are high, *i.e.* essentially at the beginning of
 506 drying near the exposed surfaces. Note that in practice, due to cyclic and seasonal environmental
 507 conditions, significant gradients may persist in these zones, meaning that the involved
 508 aggregates may have a certain impact on the kinetics.



509

510

511

512 *Figure 17 – saturation degree profiles as a function of the radius for the 6 calculated specimens at 3 different*
 513 *times.*

514 Overall, considering all the other factors as constant, the variability in the (coarse) aggregate
 515 distribution as investigated here cannot explain the dispersion observed experimentally in the
 516 fieldcrete (and also to a lesser extent in the labcrete) specimens. Some other reasons should be
 517 pointed out, as the variability in the formulation and in the phase properties of the cement paste.
 518 To be addressed, these aspects would need to be characterized experimentally, which
 519 constitutes a challenging aspect.

520

521 5. Conclusion

522 In order to characterize the difference in permeability between labcrete and fieldcrete, the
523 unsaturated permeability to water of a modern concrete was evaluated using inverse analysis.
524 Labcrete specimens were prepared and cured in the laboratory and fieldcrete specimens were
525 prepared during the construction of test panels (ca 25m³). The fieldcrete appeared to be more
526 porous than the labcrete (11.9% in average vs. 10.6%) but, using inverse analysis and
527 accounting for water permeation only, the intrinsic permeability values were very close for the
528 two concretes (2.2×10^{-22} and 2.1×10^{-22} in average for the labcrete and fieldcrete, respectively).
529 The fieldcrete however exhibited lower pore-interaction factor (*i.e.* the parameter of Mualem's
530 model that accounts for pore structure tortuosity and connectivity) than the labcrete (-1.2 vs. -
531 0.56), indicating that the tortuosity and connectivity of the poral network were not the same for
532 the two concretes. The fieldcrete also displayed more scatter, which can be mainly attributed to
533 the five distinct batches that were considered. Clearly enough, non-negligible discrepancies were
534 reported in the identified relative permeabilities for the two concretes, in particular for
535 saturation degrees below about 0.7. These differences increased for decreasing values of
536 saturation, the relative permeability of fieldcrete remaining higher. This means that the drying
537 kinetics of fieldcrete would be potentially faster for low saturation, but in practical
538 environmental conditions such small saturation states are likely to be rarely met.

539 Moreover, one-dimensional simulations performed on a saturated homogeneous concrete wall
540 subjected to drying at HR=55% showed very little differences between fieldcrete and labcrete
541 (with model parameters prescribed as the averaged ones) in terms of saturation degree profiles
542 at various times. By contrast, important variations were observed when the parameters
543 identified on the various fieldcrete specimens were successively considered in the calculations.
544 Finally, as a first attempt to investigate the effects of the aggregate distribution on the variability
545 observed on the experimental results, 3D mesoscale simulations were carried out on
546 reconstructed cylindrical specimens of same dimensions as the tested ones. Only the aggregate

547 distributions and shapes were varied between the 3 generated cubes where the 6 samples were
548 cored. This resulted in slight variations of aggregate volume fraction between the specimens.
549 Overall, the main results indicated that the evolutions of volume-averaged saturation degrees
550 and surface-averaged saturation degree profiles were almost identical for all 6 specimens. Only
551 by examining the saturation degree at given distances from the exposed surface along the axis
552 direction of the samples can be observed non-negligible variations, in particular near the surface
553 where the saturation gradients are higher. This means that the different aggregate distributions
554 between numerical specimens lead to significant local saturation disparities, but cannot alone
555 explain the observed macroscopic variability. An important part may originate from the matrix
556 properties themselves (*i.e.* spatial variability in the content, the porosity, the placement etc.),
557 which are however quite difficult to characterize experimentally. This aspect would deserve to
558 be addressed, both on the numerical and experimental grounds.

559 Acknowledgments

560 This work could be done thanks to the financial support of the Belgian Agency for Radioactive
561 Waste and Enriched Fissile Materials (ONDRAF·NIRAS) and the French Alternative Energies and
562 Atomic Energy Commission (CEA).

563 5. References

- 564 [1] A. Abbas, M. Carcasses, J.-P. Ollivier, Gas permeability of concrete in relation to its degree
565 of saturation, *Mater. Struct.* 32 (1999) 3–8. doi:10.1007/BF02480405.
- 566 [2] J.P. Monlouis-Bonnaire, J. Verdier, B. Perrin, Prediction of the relative permeability to gas
567 flow of cement-based materials, *Cem. Concr. Res.* 34 (2004) 737–744.
568 doi:10.1016/S0008-8846(03)00071-1.
- 569 [3] J. Sercombe, R. Vidal, C. Gallé, F. Adenot, Experimental study of gas diffusion in cement
570 paste, *Cem. Concr. Res.* 37 (2007) 579–588. doi:10.1016/j.cemconres.2006.12.003.
- 571 [4] N. Olsson, V. Baroghel-Bouny, L.O. Nilsson, M. Thiery, Non-saturated ion diffusion in
572 concrete - A new approach to evaluate conductivity measurements, *Cem. Concr. Compos.*
573 40 (2013) 40–47. doi:10.1016/j.cemconcomp.2013.04.001.
- 574 [5] Y. Zhang, M. Zhang, Transport properties in unsaturated cement-based materials - A
575 review, *Constr. Build. Mater.* 72 (2014) 367–379.
576 doi:10.1016/j.conbuildmat.2014.09.037.

- 577 [6] K. Tuutti, Corrosion of steel in concrete, CBI Report 4.82, Swedish Cement and Concrete
578 Research Institute, Stockholm (Sweden), 1982. doi:10.4324/9780203414606_chapter_2.
- 579 [7] H.J. Wierig, Long-term studies on the carbonation of concrete under normal outdoor
580 exposure, in: R.C.P.C. CPC14 (Ed.), Rilem Semin. Durab. Concr. Struct. under Norm.
581 Outdoor Expo., Rilem, Hannover (Germany), 1984: pp. 239–249.
- 582 [8] I. Galan, C. Andrade, M. Castellote, Natural and accelerated CO₂ binding kinetics in cement
583 paste at different relative humidities, *Cem. Concr. Res.* 49 (2013) 21–28.
584 doi:10.1016/j.cemconres.2013.03.009.
- 585 [9] Z.P. Bažant, W.J. Raftshol, Effect of cracking in drying and shrinkage specimens, *Cem.*
586 *Concr. Res.* 12 (1982) 209–226.
- 587 [10] B. Bissonnette, P. Pierre, M. Pigeon, Influence of key parameters on drying shrinkage of
588 cementitious materials, *Cem. Concr. Res.* 29 (1999) 1655–1662. doi:10.1016/S0008-
589 8846(99)00156-8.
- 590 [11] S.P. Shah, W.J. Weiss, W. Yang, Shrinkage Cracking - Can It Be Prevented?, *Concr. Int.* 20
591 (1998) 51–55.
- 592 [12] V. Baroghel-Bouny, Evaluation and prediction of reinforced concrete durability by means
593 of durability indicators. Part I: new performance-based approach, in: K. Kovler (Ed.),
594 *Concr. - Int. RILEM-JCI Semin. Concr. Durab. Serv. Life Plan. Curing, Crack Control.*
595 *Perform. Harsh Environ., RILEM Pro46, Ein-Bokek (Israel), 2006: pp. 259–269.*
596 doi:10.1617/291214390X.028.
- 597 [13] V. Baroghel-Bouny, T.Q. Nguyen, P. Dangla, Assessment and prediction of RC structure
598 service life by means of durability indicators and physical/chemical models, *Cem. Concr.*
599 *Compos.* 31 (2009) 522–534. doi:10.1016/j.cemconcomp.2009.01.009.
- 600 [14] M. Alexander, M. Thomas, Service life prediction and performance testing - Current
601 developments and practical applications, *Cem. Concr. Res.* 78 (2015) 155–164.
602 doi:10.1016/j.cemconres.2015.05.013.
- 603 [15] M. Carcasses, L. Linger, F. Cussigh, P. Rougeau, F. Barberon, B. Thauvin, F. Cassagnabere, J.
604 Mai-Nhu, M. Dierkens, M.-P. Cubaynes, Setting up of a database dedicated to durability
605 indicators by the Civil Works French Association (AFGC) to support the implementation
606 of concrete performance-based approach, in: *Fib Symp., FIB, Copenhagen (Denmark),*
607 2015: pp. 1–11.
- 608 [16] G. Nganga, M. Alexander, H. Beushausen, Practical implementation of the durability index
609 performance-based design approach, *Constr. Build. Mater.* 45 (2013) 251–261.
610 doi:10.1016/j.conbuildmat.2013.03.069.
- 611 [17] A.M. Vaysburd, C.D. Brown, B. Bissonnette, P.H. Emmons, “Realcrete versus labcrete”
612 searching for tests that give reliable results, *Concr. Int.* 26 (2004) 90–94.
- 613 [18] R.J. Torrent, Service Life Prediction : Theorecrete, Labcrete and Realcrete Approaches, in:
614 P.A. Claisse (Ed.), *Proc. 3rd Int. Conf. Sustain. Constr. Mater. Technol., Kyoto (Japan),*
615 2013: pp. 1–18.
- 616 [19] A. Neville, The question of concrete durability: we can make good concrete today, *Concr.*
617 *Int.* 22 (2000) 21–26.
- 618 [20] B.A. Suprenant, Dealing with the ‘labcrete-realcrete’ gap, *Concr. Prod.* January (1998) 37–
619 40.
- 620 [21] R.L. Blick, C.F. Petersen, M.E. Winter, Proportioning and controlling high-strength

- 621 concrete, ACI Spec. Publ. 46 (1974) 141–163.
- 622 [22] F. Cussigh, V. Bonnard, C. Carde, O. Houdusse, Rion Antirion bridge project - concrete
623 durability towards corrosion risk, in: F. Toutlemonde, K. Sakai, O.E. Gjorv, N. Banthia
624 (Eds.), Proc. 5th Int. Conf. Concr. under Sev. Cond. Environ. Load., LCPC, Tours (France),
625 2007: pp. 839–850.
- 626 [23] V. Baroghel-Bouny, M. Dierkens, X. Wang, A. Soive, M. Saillio, M. Thiery, B. Thauvin, Ageing
627 and durability of concrete in lab and in field conditions: investigation of chloride
628 penetration, *J. Sustain. Cem. Mater.* 2 (2013) 67–110.
- 629 [24] R.D. Neves, J. Vinagre Santos, Air permeability assessment in a reinforced concrete
630 viaduct, in: Proc. Int. RILEM Conf. Site Assess. Concr. Mason. Timber Struct., Como Lake,
631 Italy, 2008: pp. 299–307.
- 632 [25] S. Poyet, X. Bourbon, Experimental Investigation of Concrete Packages for Radioactive
633 Waste Management: Permeability and Influence of Junctions, *Transp. Porous Media.* 95
634 (2012) 55–70. doi:10.1007/s11242-012-0032-y.
- 635 [26] R. Neves, F. Branco, J. De Brito, Field assessment of the relationship between natural and
636 accelerated concrete carbonation resistance, *Cem. Concr. Compos.* 41 (2013) 9–15.
637 doi:10.1016/j.cemconcomp.2013.04.006.
- 638 [27] E. Diaz, F. Martirena, A. Alujas, R. Torrent, Low Carbon Cement: durability performance
639 assessment with laboratory and site tests, in: K.L. Scrivener, A. Favier (Eds.), Proc. 1st Int.
640 Conf. Calcined Clays (Calcined Clays Sustain. Concr., Springer, 2015: pp. 277–282.
- 641 [28] S. Starck, H. Beushausen, M. Alexander, R. Torrent, Complementarity of in situ and
642 laboratory-based concrete permeability measurements, *Mater. Struct. Constr.* 50 (2017)
643 4–7. doi:10.1617/s11527-017-1037-3.
- 644 [29] H. Saricimen, M. Maslehuddin, A.J. Al-Tayyib, A.I. Al-Mana, Permeability and durability of
645 plain and blended cement concretes cured in field and laboratory conditions, *ACI Mater. J.*
646 92 (1995) 111–116.
- 647 [30] W.R. Malisch, How producers can correct improper test-cylinder curing, *Concr. Prod.*
648 November (1997) 782–784.
- 649 [31] M. Castellote Armero, C. Andrade Perdrix, A. Castillo Talavera, Characterization and
650 properties of cementitious matrices for a surface disposal of LLW, Eduardo Torroja
651 Institute (IETcc), report 19.171, 98p, Madrid (Spain), 2009.
- 652 [32] J. Piérard, E. Coppens, Sensitiviteitsstudie op beton (in Dutch), CSTC Report DE65092004,
653 Brussels (Belgium), 2011.
- 654 [33] P.C. Kreijger, The skin of concrete Composition and properties, *Mater. Struct.* 17 (1990)
655 275–283.
- 656 [34] J.M. Khatib, P.S. Mangat, Absorption characteristics of concrete as a function of location
657 relative to casting position, *Cem. Concr. Res.* 25 (1995) 999–1010.
- 658 [35] J.M. Khatib, P.S. Mangat, Porosity of cement paste cured at 45 °C as a function of location
659 relative to casting position, *Cem. Concr. Compos.* 25 (2003) 97–108.
- 660 [36] J.M. Khatib, S. Kenai, J.S. Zhang, S. Firat, P.H. Harris, Effect of Sample Location and Curing
661 on Pore Volume and Threshold Diameter of Cement Paste with and without Slag, in: J.
662 Zachar, P. Claisse, T.R. Naik, E. Ganjian (Eds.), Proc. 2nd Int. Conf. Sustain. Constr.
663 Technol., Ancona (Italy), 2010: pp. 1–9.
- 664 [37] AFNOR, Essai pour béton durci : essai de porosité et de masse volumique (in French),

- 665 Stand. NF P18-459. (2010) 9p.
- 666 [38] M. Mainguy, O. Coussy, V. Baroghel-Bouny, Role of air pressure in drying of weakly
667 permeable materials, *J. Eng. Mech.* 127 (2001) 592–592.
- 668 [39] O. Coussy, *Poromechanics*, John Wiley & Sons, Ltd, Chichester (England), 2004.
- 669 [40] M. Bocciarelli, G. Ranzi, Identification of the hygro-thermo-chemical-mechanical model
670 parameters of concrete through inverse analysis, *Constr. Build. Mater.* 162 (2018) 202–
671 214. doi:10.1016/j.conbuildmat.2017.11.167.
- 672 [41] S. Poyet, S. Charles, N. Honoré, V. L'Hostis, Assessment of the unsaturated water transport
673 properties of an old concrete: Determination of the pore-interaction factor, *Cem. Concr.*
674 *Res.* 41 (2011) 1015–1023. doi:10.1016/j.cemconres.2011.06.002.
- 675 [42] S. Poyet, Determination of the intrinsic permeability to water of cementitious materials:
676 Influence of the water retention curve, *Cem. Concr. Compos.* 35 (2013) 127–135.
677 doi:10.1016/j.cemconcomp.2012.08.023.
- 678 [43] M.T. van Genuchten, A Closed-form Equation for Predicting the Hydraulic Conductivity of
679 Unsaturated Soils, *Soil Sci. Soc. Am. J.* 44 (1980) 892–898.
680 doi:10.2136/sssaj1980.03615995004400050002x.
- 681 [44] A. Aït-Mokhtar, R. Belarbi, F. Benboudjema, N. Burlion, B. Capra, M. Carcassès, J.-B. Colliat,
682 F. Cussigh, F. Deby, F. Jacquemot, T. de Larrard, J.-F. Lataste, P. Le Bescop, M. Pierre, S.
683 Poyet, P. Rougeau, T. Rougelot, A. Sellier, J. Séménadisse, J.-M. Torrenti, A. Trabelsi, P.
684 Turcry, H. Yanez-Godoy, Experimental investigation of the variability of concrete
685 durability properties, *Cem. Concr. Res.* 45 (2013) 21–36.
686 doi:10.1016/j.cemconres.2012.11.002.
- 687 [45] A. Trabelsi, P. Turcry, R. Belarbi, Water vapour desorption variability of in situ concrete
688 and effects on drying simulations, *Mag. Concr. Res.* 63 (2011) 333–342.
689 doi:10.1680/mac9.00161.
- 690 [46] B.M. Savage, D.J. Janssen, Soil Physics Principles Validated for Use in Predicting
691 Unsaturated Moisture Movement in Portland Cement Concrete, *ACI Mater. J.* 94 (1997)
692 63–70. doi:10.14359/286.
- 693 [47] Y. Mualem, A new model for predicting the hydraulic conductivity of unsaturated porous
694 media, *Water Resour. Res.* 12 (1976) 513–522.
695 doi:http://doi.wiley.com/10.1029/WR012i003p00513.
- 696 [48] J.H.M. Wösten, M.T. van Genuchten, Using texture and other soil properties to predict the
697 unsaturated soil hydraulic functions, *Soil Sci. Soc. Am. J.* 52 (1988) 1762–1770.
- 698 [49] W.M. Schuh, R.L. Cline, Effect of soil properties on unsaturated hydraulic conductivity
699 pore-interaction factors, *Soil Sci. Soc. Am. J.* 54 (1990) 1509–1519.
- 700 [50] K. Kosugi, General model for unsaturated hydraulic conductivity for soils with lognormal
701 pore-size distribution, *Soil Sci. Soc. Am. J.* 63 (1999) 270–277.
- 702 [51] J.A. Vrugt, P.H. Stauffer, T. Wohling, B.A. Robinson, V. V. Vesselinov, Inverse Modeling of
703 Subsurface Flow and Transport Properties: A Review with New Developments, *Vadose Zo.*
704 *J.* 7 (2008) 843–864. doi:10.2136/vzj2007.0078.
- 705 [52] K.S. Zadeh, Parameter estimation in flow through partially saturated porous materials, *J.*
706 *Comput. Phys.* 227 (2008) 10243–10262. doi:10.1016/j.jcp.2008.09.007.
- 707 [53] Q. Niu, D. Fratta, Y.-H. Wang, The use of electrical conductivity measurements in the
708 prediction of hydraulic conductivity of unsaturated soils, *J. Hydrol.* 522 (2015) 475–487.

- 709 doi:10.1016/j.jhydrol.2014.12.055.
- 710 [54] M.G. Schaap, F.J. Leij, Improved prediction of unsaturated hydraulic conductivity with the
711 Mualem-van Genuchten model, *Soil Sci. Soc. Am. J.* 64 (2000) 843–851.
- 712 [55] R. Sommer, H. Folster, K. Vielhauer, E.J.M. Carvalho, P.L.G. Vlek, Deep Soil Water Dynamics
713 and Depletion by Secondary Vegetation in the Eastern Amazon, *Soil Sci. Soc. Am. J.* 67
714 (2003) 1672–1686. doi:10.2136/sssaj2003.1672.
- 715 [56] G. Wardeh, B. Perrin, Relative permeabilities of cement-based materials: influence of the
716 tortuosity function, *J. Build. Phys.* 30 (2006) 39–57.
- 717 [57] C. Leech, D. Lockington, R.D. Hooton, G. Galloway, G. Cowin, P. Dux, Validation of Mualem’s
718 Conductivity Model and Prediction of Saturated Permeability from Sorptivity, *ACI Mater.*
719 *J.* 105 (2008) 44–51. doi:10.14359/19206.
- 720 [58] I. Comby-Peyrot, F. Bernard, P.O. Bouchard, F. Bay, E. Garcia-Diaz, Development and
721 validation of a 3D computational tool to describe concrete behaviour at mesoscale.
722 Application to the alkali-silica reaction, *Comput. Mater. Sci.* 46 (2009) 1163–1177.
723 doi:10.1016/j.commatsci.2009.06.002.
- 724 [59] Y. Huang, Z. Yang, W. Ren, G. Liu, C. Zhang, 3D meso-scale fracture modelling and
725 validation of concrete based on in-situ X-ray Computed Tomography images using
726 damage plasticity model, *Int. J. Solids Struct.* 67–68 (2015) 340–352.
727 doi:10.1016/j.ijsolstr.2015.05.002.
- 728 [60] T. Wu, P. Wriggers, Multiscale diffusion–thermal–mechanical cohesive zone model for
729 concrete, *Comput. Mech.* 55 (2015) 999–1016. doi:10.1007/s00466-015-1149-y.
- 730 [61] X. Li, S. Chen, Q. Xu, Y. Xu, Modeling the three-dimensional unsaturated water transport in
731 concrete at the mesoscale, *Comput. Struct.* 190 (2017) 61–74.
732 doi:10.1016/j.compstruc.2017.05.005.
- 733 [62] T. de Larrard, B. Bary, E. Adam, F. Kloss, Influence of aggregate shapes on drying and
734 carbonation phenomena in 3D concrete numerical samples, *Comput. Mater. Sci.* 72 (2013)
735 1–14. doi:10.1016/j.commatsci.2013.01.039.
- 736 [63] T.T.H. Nguyen, B. Bary, T. De Larrard, Coupled carbonation-rust formation-damage
737 modeling and simulation of steel corrosion in 3D mesoscale reinforced concrete, *Cem.*
738 *Concr. Res.* 74 (2015) 95–107. doi:10.1016/j.cemconres.2015.04.008.
- 739 [64] B. Bary, C. Bourcier, T. Helfer, Analytical and 3D numerical analysis of the
740 thermoviscoelastic behavior of concrete-like materials including interfaces, *Adv. Eng.*
741 *Softw.* 112 (2017) 16–30. doi:10.1016/j.advengsoft.2017.06.006.
- 742 [65] F. Bernachy-Barbe, B. Bary, “Effect of aggregate shapes on local fields in 3D mesoscale
743 simulations of the concrete creep behavior,” *Finite Elements in Analysis and Design*, 156
744 (2019), pp. 13–23.
- 745
- 746